Journal of Electronic Materials (2023) 52:6730–6740
https://doi.org/10.1007/s11664-023-10614-4

ORIGINAL RESEARCH ARTICLE

Orthorhombic-Nb_2O_5 Nanocrystal@carbon Hybrid Spheres as Anode Material for Enhanced Lithium-Ion Storage

Yonghui Lin[1,2] · Wei Lv[1,2] · Yongfeng Yuan[2] · Congwei Wang[2] · Zhouyu Huang[2]

Received: 16 May 2023 / Accepted: 14 July 2023 / Published online: 28 July 2023

Abstract

Orthorhombic Nb_2O_5 (T-Nb_2O_5) nanocrystal@carbon hybrid spheres were synthesized *via* the controlled hydrolysis of niobium ethoxide, the assembly effect of oleylamine, and subsequent carbonization. The size of the T-Nb_2O_5 nanocrystals was ~ 26.6 nm, and the diameter of the hybrid spheres was 300–400 nm. The contents of T-Nb_2O_5 and carbon were 87.84% and 11.91%, respectively. The hybrid spheres exhibited excellent Li storage performance, including high reversible capacity (447 mAh g^{-1} at 0.5 A g^{-1}/2.5C), good rate capability (186 mAh g^{-1} at 5 A g^{-1}/25C), and excellent cycling stability (279 mAh g^{-1} after 600 cycles at 1 A g^{-1}/5C). The capacity decay rate was only 0.06% per cycle. It has been found that the electrochemical performance of the hybrid spheres is superior to those of other reported Nb_2O_5 composites. Moreover, the reaction kinetics of the hybrid spheres are also outstanding. The impedance is low, while the Li^+ diffusion coefficient is high. The hybrid spheres maintain good structural integrity after 600 cycles. The superior Li storage performance is associated with the unique architecture of the hybrid spheres. The ultrafine size of Nb_2O_5 nanocrystals ensures high electrochemical activity. The surface carbon and internal carbon of the hybrid spheres not only protect Nb_2O_5 but also promote the rapid transfer of electrons and Li^+. These results demonstrate that T-Nb_2O_5 nanocrystal@carbon hybrid spheres are a promising candidate material for lithium-ion storage.

Graphical Abstract

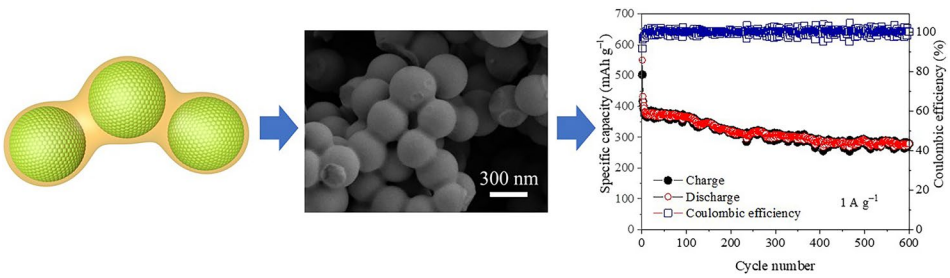

T-Nb_2O_5 nanocrystal@carbon hybrid spheres

Keywords Lithium-ion batteries · Nb_2O_5 · carbon · hybrid sphere

Introduction

With the rapid development of portable electronics, electric vehicles, and smart grids, higher and higher requirements are put forward for lithium-ion batteries (LIBs). Unfortunately, graphite, as the dominant commercial anode material, has become a serious technical bottleneck because of its limited rate performance, low theoretical

✉ Yongfeng Yuan
yuanyf@zstu.edu.cn

[1] Zhejiang Ecowell Energy Management Technology Co., Ltd., Hangzhou 310012, Zhejiang, China

[2] College of Machinery Engineering, Zhejiang Sci-Tech University, Hangzhou 310018, China

capacity, and certain safety risks.[1–4] It is urgent to develop new advanced anode material with high reversible capacity, excellent rate capability, long lifespan, and high safety.[5–8] As a typical pseudocapacitive material, Nb_2O_5 has attracted much attention due to the fast Li^+ diffusion, small volume change (< 3%), high lithiation potential (~1.6 V vs. Li/Li^+), and high theoretical capacity (200 mAh g^{-1}).[9–12] In high-rate and high-security applications, Nb_2O_5 is considered to be one of the most excellent candidates.[13] Despite these advantages, the band gap of Nb_2O_5 is relatively wide, ~ 3.2 eV, which leads to a low electronic conductivity, only 3.4×10^{-6} S cm^{-1}, which limits its lithium storage performance and hinders its practical application.[14,15]

To overcome the inherent shortcomings of Nb_2O_5, numerous strategies have been investigated. One common method is nanostructure engineering. Decreasing the particle size of Nb_2O_5 can shorten the distances of ion diffusion and electron transport, and improve the reaction kinetics to a certain extent.[16,17] So far, many Nb_2O_5 nanomaterials, such as nanosheets,[18] mesoporous microspheres,[19] flowers,[20] and nanorod films,[21] have been reported. However, pure Nb_2O_5 nanomaterials tend to aggregate, and the large specific surface area easily induces serious side reactions and poor stability. These limitations compromise the structural advantages of Nb_2O_5 nanomaterials. Compared with pure nanomaterials, the composite of Nb_2O_5 with conductive materials, such as carbon, is another more attractive strategy. The composite can improve the electronic conductivity and cycling durability of Nb_2O_5, and avoid the aggregation of Nb_2O_5 nanomaterials.[22–24] In the field of Nb_2O_5/carbon nanocomposites, much progress has been achieved. For example, Yu et al. synthesized Nb_2O_5 nanosheets/graphene composites, which delivered a reversible capacity of 292 mAh g^{-1} at 1 C after 70 cycles.[25] Zhu et al. prepared Al-doped Nb_2O_5/carbon microparticles and obtained a reversible capacity of 267 mAh g^{-1} at 2 A g^{-1} after 300 cycles.[26] Chen et al. synthesized carbon-coated microsized hexagonal TT-Nb_2O_5 composites and achieved a specific capacity of 228 mAh g^{-1} at 0.2 C.[27] Nevertheless, Nb_2O_5 nanocomposites still face many challenges. For most Nb_2O_5 nanocomposites, it is very difficult to control the irreversible side reactions because the large surface area of the nanomaterials easily results in the constant consumption of electrolytes to generate solid electrolyte interface (SEI) film during long-term charge–discharge cycles, which brings about a decline in the capacity of Nb_2O_5. Therefore, the rational design of the Nb_2O_5 nanocomposite structure is crucial. Embedding Nb_2O_5 nanocrystals into a carbon matrix is a good strategy to overcome this problem. However, the strategy is very challenging. The difficulty lies in precise control of Nb_2O_5 size and carbon content as well as the rational construction of the composite structures.

Here, we have chosen orthorhombic Nb_2O_5 (T-Nb_2O_5) as the object. Compared with other crystal structures of Nb_2O_5, T-Nb_2O_5 is a typical and unique pseudocapacitive material. Li ions can be transported rapidly in two dimensions without phase transition during the lithiation/delithiation process.[28] This endows T-Nb_2O_5 with a satisfactory rate performance and specific capacity. A facile assembling strategy was developed to construct the hybrid spheres of T-Nb_2O_5 and amorphous carbon (denoted as T-Nb_2O_5@CS) through the controlled hydrolysis of niobium (V) ethoxide, as well as the intensive adsorption of oleylamine, followed by a simple carbonization. This synthesis method can control the particle size of Nb_2O_5 to a very small nanoscale, avoid the direct contact between Nb_2O_5 nanocrystals with electrolyte to form stable SEI films, and construct high-speed transmission channels for electrons and Li^+. Benefitting from the well-organized composite structure, the resulting T-Nb_2O_5@CS has an excellent lithium storage performance. After 600 cycles at a current density of 1 A g^{-1}, a reversible capacity of 279 mAh g^{-1} has been obtained. Even at 5 A g^{-1}, the average discharge capacity was still as high as 186 mAh g^{-1}. This work paves an effective way for the design and synthesis of high-performance Nb_2O_5 nanocomposites.

Experimental

Materials Preparation

In a typical synthesis, 0.1 mL of niobium ethoxide was injected into a mixed solution of 5 mL of oleylamine and 60 mL of anhydrous ethanol. Then, the beaker was sealed with preservative film and vigorously stirred for 2 h. The precipitate was washed with anhydrous ethanol several times, and the centrifuged products were dried at 80°C in a vacuum oven overnight, and then placed in a quartz tube, purged with Ar, and heated to 700°C for 2 h at 2°C min^{-1}.

Materials Characterizations

X-ray powder diffraction (XRD) patterns were recorded with an D8 Advance (Bruker) x-ray diffractometer with a Cu Kα ray as the light source (λ = 1.5406 Å). Transmission electron microscopy (TEM) and high-resolution (HR) TEM images were obtained by JEM-2100 (JEOL) electron microscope operating at 200 kV. Field-emission scanning electron microscopy (SEM) images and elemental mapping were collected an S4800 (Hitachi) electron microscope. X-ray photoelectron spectroscopy (XPS) measurements were conducted on an ESCALAB-MK (VG) with Al Kα radiation ($h\nu$ = 1486.6 eV) as the x-ray source. Thermogravimetric analyses (TGA) were performed in order to study the thermal decomposition of the product by a TG209F3

(NETZSCH) analyzer with 10°C min^{-1} in air flow. Raman spectra were recorded using a spectrometer (HR Evolution; LabRAM) with 532-nm laser excitation.

Electrochemical Measurements

The electrochemical performances were investigated on CR2025 coin cells with T-Nb_2O_5@CS as the anode, lithium foil as the reference/counter electrode, and polypropylene film (Celgard 2400) as the separator. An amount of 1 M $LiPF_6$ in diethyl carbonate/ethylene carbonate binary solvents (1:1 by volume) was used as the electrolyte, and 0.2 ml of electrolyte was added into each cell. The coin cells were assembled in a high-purity argon-filled glovebox. The working electrodes were prepared by spreading the slurry on Cu foils with a diameter of 12 mm. The slurry was composed of the active material, polyvinylidene fluoride, and super P, with a mass ratio of 80:10:10. The slurry was ground in N-methyl-2-pyrrolidinone. The working electrodes were dried at 90°C under vacuum. The mass of the active material was controlled at ~ 1.0 mg cm^{-2}. A NEWARE battery test system was used to carry out the galvanostatic charge/discharge and rate performance, using the galvanostatic intermittent titration technique (GITT). Cyclic voltammetry (CV) curves were recorded between 0.01 V and 3.0 V with an electrochemical workstation (PARSTAT 2273). Electrochemical impedance spectroscopy (EIS) measurements were conducted on the same workstation with a 5-mV AC amplitude. The frequency range was 10^5–10^{-2} Hz.

Results and Discussion

The synthetic process of T-Nb_2O_5@CS is schematically illustrated in Fig. 1. First, a small amount of niobium ethoxide and a certain amount of oleylamine were dissolved in a great deal of anhydrous ethanol to form a homogenous solution. The niobium ethoxide was sufficiently diluted, which is very conducive to reducing the particle size of the hydrolysis product. In addition, the hydrolysis reaction of niobium ethoxide was induced by moisture in the air. Through controlling the diffusion rate of moisture into the beaker, the hydrolysis of the niobium ethoxide was further limited. The synergistic effect of the above factors achieved the extremely slow hydrolysis of the niobium ethoxide and ensured the nanoscale size of the hydrolysis product. Due to the strong adsorption and high stickiness of the oleylamine, the hydrolysis products could be immediately coated by the oleylamine, and further assembled into large hierarchical spheres. Finally, the oleylamine was decomposed into carbon by calcination. The formed carbon can inhibit the growth of Nb_2O_5 nanocrystals at high temperature, which maintains their high activity. The formed carbon also constructs conductive frameworks inside the hybrid spheres, which remarkably improves the electronic conductivity of Nb_2O_5.

Figure 2a shows an SEM image of the precursors (hydrolysis product), which are uniform small spheres with smooth surfaces with a diameter of 300–400 nm. Several small spheres are bonded together by a thin layer of amorphous material, oleylamine. This can be demonstrated by the fracture on a small ball. In the TEM image (Fig. 2b), these small spheres exhibit a dense and homogenous internal structure. The oleylamine between the small spheres is semitransparent, which differs from the internal dense structure of the small spheres. This coincides with the amorphous nature of oleylamine. The calcined product (T-Nb_2O_5@CS) is shown in Fig. 2c and d. The uniform and smooth small spheres are well retained without any structural deterioration. The enlarged local TEM image (Fig. 2e) indicates that a layer of amorphous carbon covers the small spheres. The thickness of the carbon layer is about several nanometers. It is difficult to distinguish the internal microstructure of the small spheres due to their high density. In the HRTEM image (Fig. 2f), the surface of the small sphere presents well-defined lattice fringes with a D-spacing of 0.39 nm, which is well matched by the (001) crystal plane of the orthorhombic Nb_2O_5 and indicates the high crystallinity of the T-Nb_2O_5

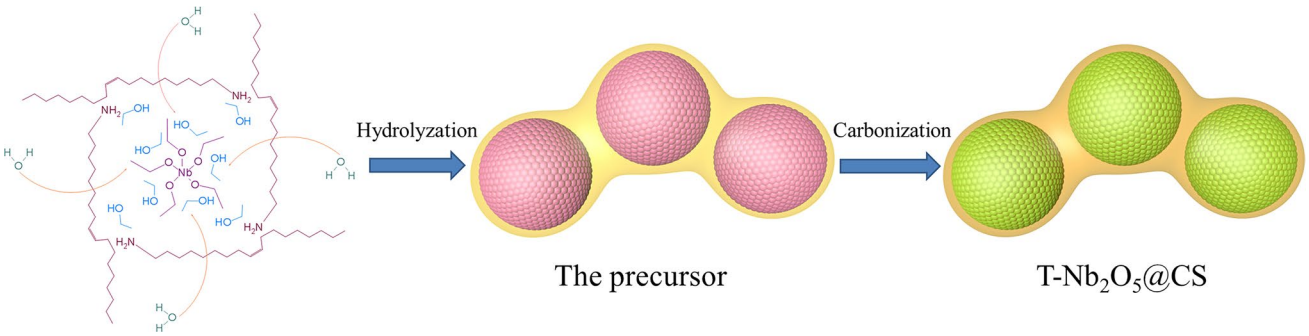

Fig. 1 Scheme of the preparation process of T-Nb_2O_5@CS.

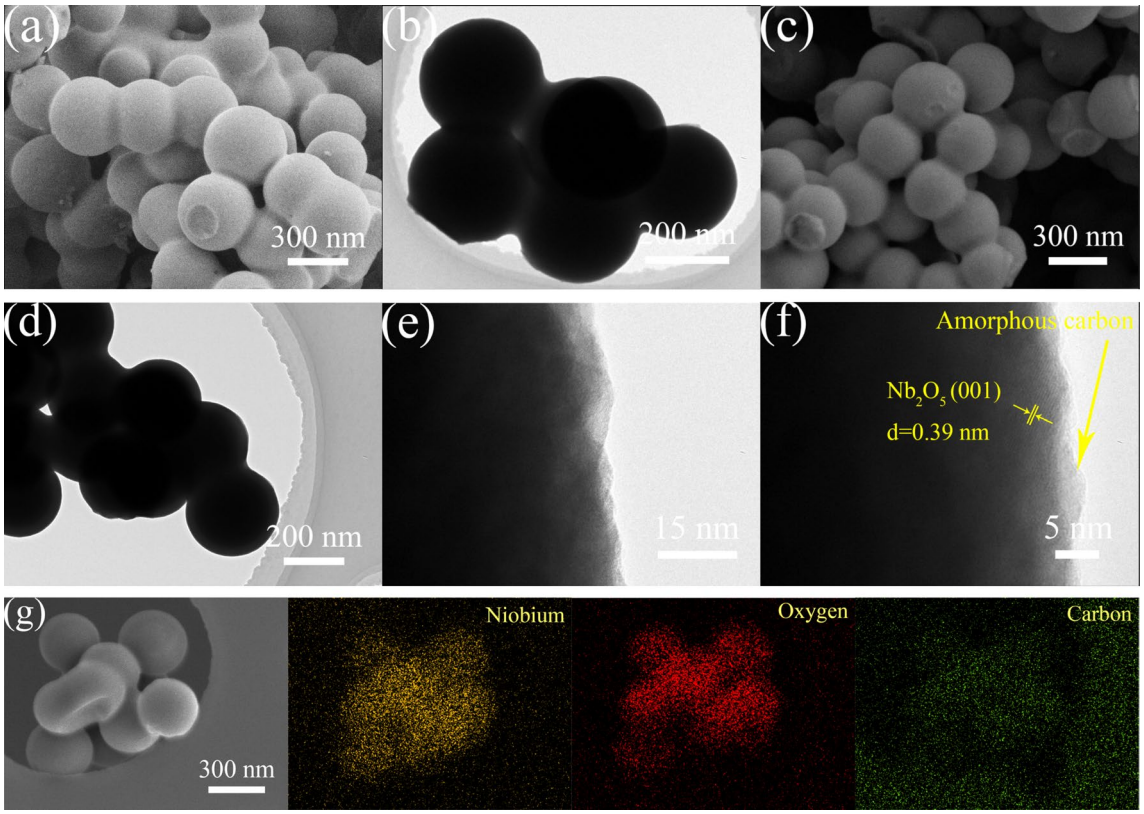

Fig. 2 (a) SEM and (b) TEM images of the precursor (hydrolysis product), (c) SEM, (d) TEM, (e) local TEM, and (f) HRTEM images of T-Nb_2O_5@CS, (g) SEM image and corresponding EDS element mappings of T-Nb_2O_5@CS.

nanocrystals. Moreover, the very thin amorphous carbon can also be clearly seen on the surface. To reveal the spatial distribution of various elements, EDS elemental mapping was performed (Fig. 2g). The distribution regions of Nb and O are highly consistent with the small spheres, indicating that the Nb_2O_5 is evenly distributed inside them. The distribution region of carbon is also consistent with the small spheres. Note that the signal intensity of carbon is the same as that of the surrounding carbon support film. It is impossible that the thin carbon on the surface of the small spheres can generate such strong carbon signals, which means that there is carbon within the spheres. That is, the sphere is a hybrid material composed of Nb_2O_5 nanoparticles and carbon.

XRD has been performed to characterize the phase and crystallinity of the as-synthesized samples. Figure 3a shows the XRD pattern of the precursor. There are only a few humps, which indicates that the hydrolysis products are amorphous. The XRD pattern of the calcined products is displayed in Fig. 3b. All the diffraction peaks are well matched with the orthorhombic Nb_2O_5, according to the standard XRD card (JCPDS 30-0873). The (001) diffraction peak is the strongest, indicating that the (001) crystal plane is dominant. This is favorable for fast intercalation of Li ions because the energy barrier of the (001) plane is low and the charge transfer is rapid.[26] The diffraction peaks are also widened, implying their small crystal size. Based on the (001) diffraction peak, the average crystal size is calculated to be 26.6 nm using the Scherrer equation ($D = k\lambda/\beta\cos\theta$), where D is the average particle size, k and λ are a constant and the x-ray wavelength, respectively, β is the half-height width of the diffraction peak, and θ is the diffraction angle. The particle size of the Nb_2O_5 is much smaller than the diameter of the small spheres. This demonstrates that the small spheres are assembled by Nb_2O_5 nanocrystals, the formation of which is attributed to three aspects: (1) the hydrolysis of niobium ethoxide is suppressed, and the hydrolysis rate is very slow, (2) oleamine has a strong adsorption effect on hydrolyzed products, and (3) oleamine-derived carbon can suppress the growth of Nb_2O_5 at high temperatures. Furthermore, the pattern baseline rises in 10–40°. This phenomenon results from amorphous carbon. There are no diffraction peaks of other materials or impurities, demonstrating the thoroughness of the hydrolysis and calcination reactions. The chemical coordination structures of the final product were further characterized by Raman spectroscopy. As shown in Fig. 3c, three well-defined peaks are located at 675 cm^{-1}, 23 cm^{-1}, 3 cm^{-1} and 127 cm^{-1}, corresponding to the symmetrically TO stretching of the Nb–O bond, the T_{2U}

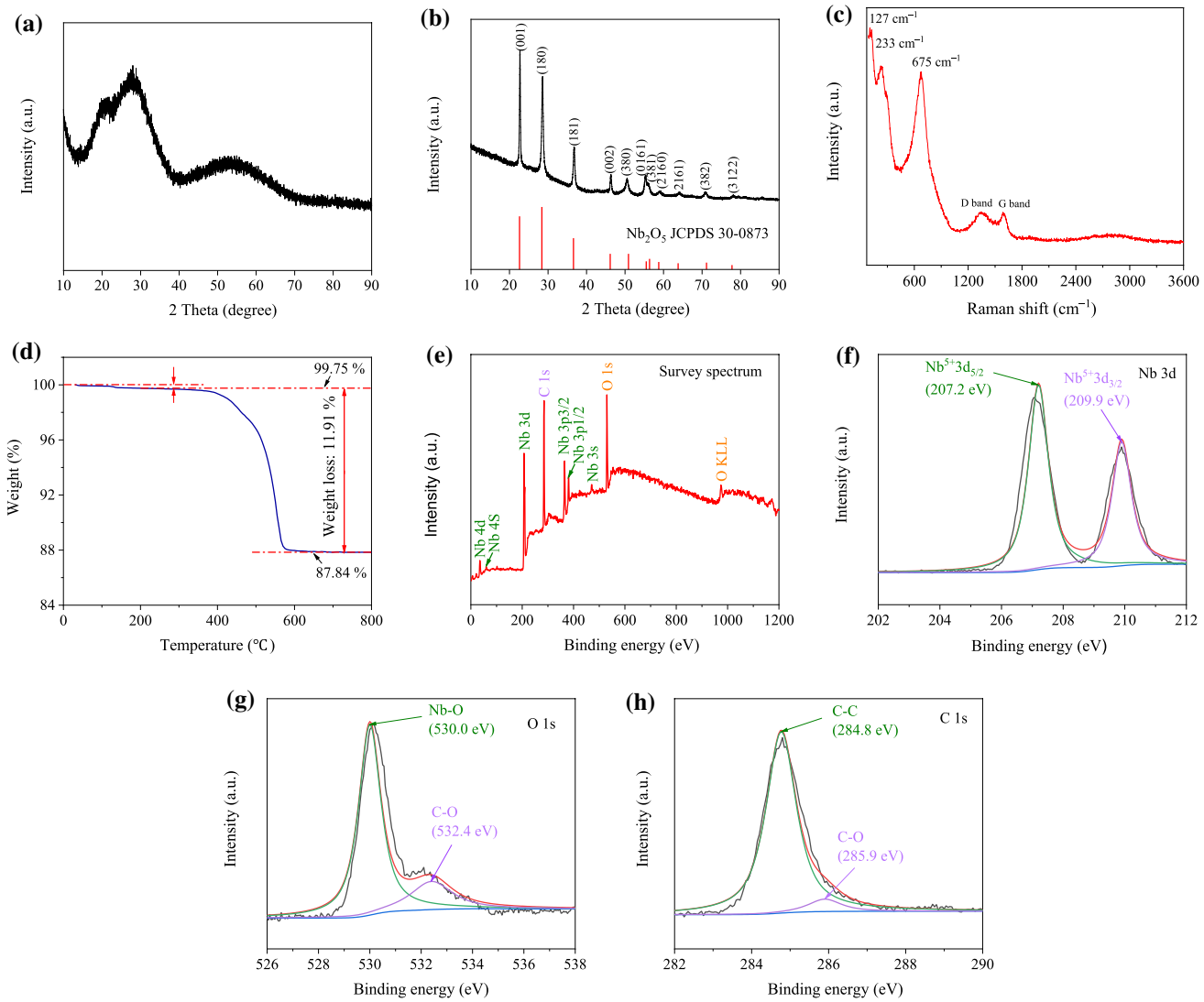

Fig. 3 XRD patterns of (a) the precursor (hydrolysis product) and (b) T-Nb_2O_5@CS, (c) Raman spectrum of T-Nb_2O_5@CS, (d) TG curve of T-Nb_2O_5@CS in air atmosphere, (e) XPS survey spectrum of T-Nb_2O_5@CS, (f) Nb 3d, (g) O 1 s, (h) C 1 s high-resolution XPS spectra of T-Nb_2O_5@CS.

bending of the Nb–O–Nb bond, and the overall vibration of the octahedra in T-Nb_2O_5, respectively.[29] The two peaks at 1340 cm^{-1} and 1590 cm^{-1} are associated with sp^2-type defect/disordered carbon in a 2D hexagonal lattice (D-band) and sp^3-type graphitic carbon (G-band). This verifies that oleamine is decomposed to carbon. The intensity ratio (I_D/I_G) was ~ 1.01. Moreover, the area of the D-band is also larger. It is believed that disordered/defective structures are dominant in the carbon matrix. That is, oleamine-derived carbon is amorphous. Note that the Raman peaks of carbon are much lower than those of Nb_2O_5, indicating that, in the hybrid spheres, amorphous carbon is the minor phase.

Under flowing air, TGA of T-Nb_2O_5@CS was carried out from 25°C to 800°C, and the resulting TGA curve is displayed in Fig. 3d. In the temperature range of 25–250°C, a negligible weight loss appears of about 0.25%, which is due to the evaporation of physically adsorbed water. A significant weight loss takes place at 250–600°C, which is attributed to the combustion of carbon to generate CO_2. The weight is stable above 600°C, and the residual mass is Nb_2O_5. According to the TGA data, it can be concluded that the contents of Nb_2O_5 and carbon are 87.84% and 11.91%, respectively. The TEM image shows that carbon on the surface of the hybrid spheres is very thin. It cannot account for 11.91%, so it is believed that most of the carbon is within the hybrid spheres.

The XPS spectra were studied to figure out the surface composition and elementary valence states of T-Nb_2O_5@CS. The XPS survey spectrum (Fig. 3e) verifies the existence of the Nb, O, and C elements. The high-resolution Nb 3d

XPS spectrum (Fig. 3f) exhibits two strong peaks centered at 207.2 eV and 209.9 eV. The spin orbit splitting energy was 2.7 eV. The two peaks are referred to Nb $3d_{5/2}$ and Nb $3d_{3/2}$. This is well consistent with the typical values of the Nb^{5+}–O bond in Nb_2O_5.[30] Figure 3g shows the high-resolution O 1s spectrum, in which two peaks are deconvoluted at 530.0 eV and 532.4 eV. The former is assigned to lattice oxygen (Nb–O) while the latter is related to loosely bonded oxygen on the hybrid spheres (C–O).[13] The C 1s high-resolution spectrum is deconvoluted to two peaks at 284.8 eV and 285.9 eV (Fig. 3h), which are associated with C–C and C–O bonds, respectively. The material characterization demonstrates that the T-Nb_2O_5@CS nanocomposite is successfully constructed on the basis of the restricted hydrolysis of niobium ethoxide and the strong stickiness of oleylamine.

The lithium storage performances were tested on the T-Nb_2O_5@CS half-cells. The first four CV curves were recorded at a scan rate of 0.2 mV s^{-1} between 0.01 V and 3.0 V (vs. Li/Li^+). As shown in Fig. 4a, the first cathodic process exhibits three distinct peaks, centered at 1.26 V, 0.61 V, and 0.01 V. They are attributed to the insertion of Li^+ into Nb_2O_5 lattices, the decomposition of the electrolyte together with the irreversible formation of SEI films, and the insertion of Li^+ into carbon, respectively. In the subsequent anodic process, the peak at 0.22 V corresponds to the extraction of Li^+ from carbon, the second peak at 0.70 V is related to the partial decomposition of the SEI film, and the third peak at 1.83 V represents the extraction of Li^+ from Nb_2O_5. In the 2nd–4th cycles, the cathodic peaks at 1.26 V and 0.61 V are coalesced into one peak, the intensity of which gradually decreases. The potential of the peak gradually shifts positively. At the same time, the anodic peak at 0.70 V also presents a decreasing intensity. These should be ascribed to the gradual stabilization of the SEI film. In the 4th cycle, both the reduction peak and the oxidation peak become wide and flat, while the CV curves are almost rectangular. These are typical features of T-Nb_2O_5 because the open framework of T-Nb_2O_5 enables Li ions to be inserted/extracted like a pseudocapacitive behavior. The electrochemical reaction of T-Nb_2O_5 can be described as follows (Eq. 1). When x is equal to 2, the theoretical capacity of T-Nb_2O_5 is ~ 200 mAh g^{-1}:

$$Nb_2O_5 + xLi^+ + xe^- \leftrightarrow Li_xNb_2O_5 (0 \le x \le 2) \quad (1)$$

Figure 4b depicts the galvanostatic discharge and charge curves of T-Nb_2O_5@CS in the first three cycles at current density of 1 A g^{-1}. The discharge and charge curves present a pair of main plateaux centered at 1.5 V/1.8 V and a pair of minor plateaux centered at 0.2 V, corresponding to the reversible Li^+ intercalation/deintercalation reactions of

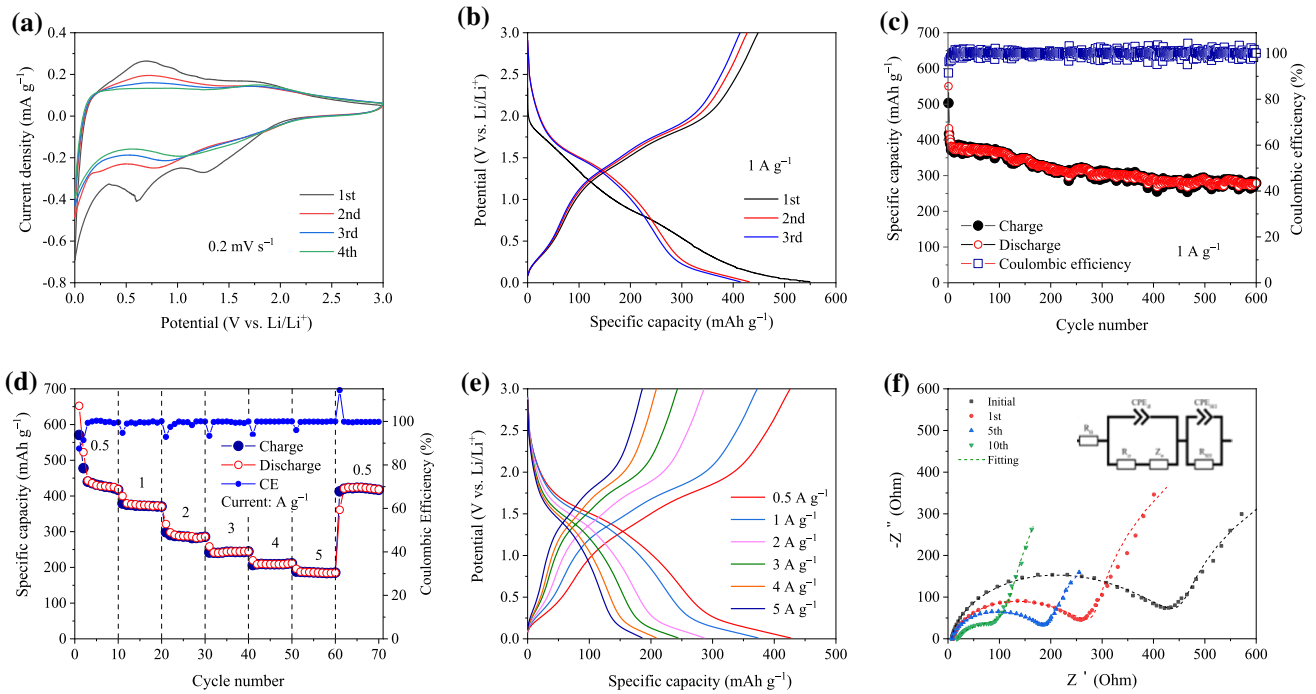

Fig. 4 (a) Cyclic voltammetry (CV) curves of T-Nb_2O_5@CS at a scan rate of 0.2 mV s^{-1}, (b) galvanostatic charge/discharge curves of T-Nb_2O_5@CS at 1 A g^{-1}, (c) long-term cycling performance of T-Nb_2O_5@CS at 1 A g^{-1}, (d) rate capability of T-Nb_2O_5@CS, (e) galvanostatic charge/discharge curves of T-Nb_2O_5@CS at different current densities, (f) Nyquist plots of T-Nb_2O_5@CS before cycling and after 1, 5, and 10 cycles.

Nb_2O_5 and carbon, respectively. The small potential hysteresis between the discharge and charge curves means a low electrode polarization, reflecting the high electronic conductivity and fast Li^+ diffusion of T-Nb_2O_5@CS. The first discharge capacity is 550 mAh g^{-1}, and the first charge capacity is 448 mAh g^{-1}. The initial coulomb efficiency (CE) was 81.4%. The irreversible formation of the SEI film is the main reason for the low initial CE. In the 2nd and 3rd cycles, the discharge–charge capacity decreases to 432/427 mAh g^{-1} and 415/413 mAh g^{-1}, but CE rises to 98.8 % and 99.5%. After the first cycle, the discharge and charge curves basically overlap, suggesting that T-Nb_2O_5@CS has good reversibility and stability.

To clarify the excellent cycling performance of T-Nb_2O_5@CS, the galvanostatic charge–discharge measurements are carried out at 1 A g^{-1}, as shown in Fig. 4c. In the first three cycles, the discharge capacity decreases from 550 mAh g^{-1} to 415 mAh g^{-1}. In the subsequent cycles, the discharge capacity decreases very slowly, exhibiting excellent stability. At the 600th cycle, T-Nb_2O_5-OV@CHS still provides a discharge capacity of 279 mAh g^{-1}. The capacity decay rate is only 0.06% per cycle with respect to the 2nd discharge. In 600 cycles, the discharge capacity of T-Nb_2O_5@CS is always higher than the theoretical value of Nb_2O_5. The additional capacity should be attributed to the pseudocapacitive effect of Nb_2O_5 and the reversible insertion/extraction of Li^+ in the gel-like SEI. CE is above 99%, except for the first several cycles, which confirms high reversibility. Compared with Nb_2O_5 anodes previously reported, the reversible capacity and cycling stability of T-Nb_2O_5@CS are better, as summarized in Table I. This convincingly demonstrates the structural superiority of T-Nb_2O_5@CS.

Figure 4d exhibits the rate performance of T-Nb_2O_5@CS at various current densities. At 0.5 A g^{-1} (2.5C), the discharge capacity drops from 571 mAh g^{-1} to 417 mAh g^{-1}. Average discharge capacity is 447 mAh g^{-1}. This demonstrates high electrochemical activity of T-Nb_2O_5@CS. This mainly benefits from the small size of the Nb_2O_5 nanocrystals. When the current density rises to 1 A g^{-1} (5 C), 2 A g^{-1} (10 C), 3 A g^{-1} (15 C), and 4 A g^{-1} (20 C), the average discharge capacity can reach 373 mAh g^{-1}, 287 mAh g^{-1}, 243 mAh g^{-1}, and 209 mAh g^{-1}, respectively. Even at a high current density of 5 A g^{-1} (25C), the average discharge capacity can still reach 186 mAh g^{-1}. The excellent rate capability is mainly ascribed to the small size of the Nb_2O_5 nanocrystals and the improvement effect of the internal conductive carbon network on the electronic conductivity of Nb_2O_5. Note that, when the current density returns to 0.5 A g^{-1}, the discharge capacity is recovered to 420 mAh g^{-1}, demonstrating the outstanding stability and reversibility of T-Nb_2O_5@CS. T-Nb_2O_5@CS is able to withstand continuous high-rate charge–discharge reactions without significant degradation. The charge–discharge curves of T-Nb_2O_5@CS at different

Table I Summary of the cycling performance of Nb_2O_5 anodes for LIBs

Materials	Current density (A g^{-1})	Specific capacity (mAh g^{-1})	Cycling number	Ref
Nb_2O_5	1	160	300	19
T-Nb_2O_5-2	0.2	178	100	20
T-Nb_2O_5 NTs-200	1	200	300	30
(AC@Nb_2O_5)/CNTs-800	1	200	40	33
N-C@MSC-Nb_2O_5	1	200	10	34
Nb_2O_5@CNTs (600℃)	1	200	10	35
PL-Nb_2O_5	1	90	300	36
NTAH	0.2	180	300	37
T-Nb_2O_5/CBG-2	0.2	216	100	38
Nb_2O_5@C	0.1	290	100	23
Nb_2O_5	1	110	200	24
M-Nb_2O_5	0.2	160	300	39
NCNTF	1	290	100	40
Nb_2O_5@rGO (2-1)	1	300	300	41
12% C–Nb_2O_5	0.2	180	200	27
M-Nb_2O_5	0.2	162	100	14
ASC/Nb_2O_5	1	90	300	42
T-Nb_2O_5/CNTs	0.1	180	300	43
Nb_2O_5	1	130	300	44
T-Nb_2O_5@CS	1	308	300	This work
		279	600	

current densities are shown in Fig. 4e. Both charge curves and discharge curves display well-defined features. Their polarization is slight, while the reaction kinetics is rapid.

To analyze the electrochemical kinetics of T-Nb_2O_5@CS, EIS was measured before cycling and after 1 cycle, 5 cycles, and 10 cycles (current density is 1 A g^{-1}). Figure 4f exhibits Nyquist plots, the fitting curves, and the equivalent circuit mode. R_{SEI} stands for the resistance of the SEI film, corresponding to the depressed semicircle in the high-frequency region. R_{ct} is the charge transfer resistance, and is related to the depressed semicircle in the medium-frequency region. Z_w represents the Warburg diffusion impedance, corresponding to an inclined line at the low-frequency region. CPE is a constant phase element. R_Ω represents the electrolyte resistance and contact resistance, equal to the intercept on the real axis. After 1 cycle, R_Ω is only 7–11 Ω. The low R_Ω is because the carbon in the hybrid spheres improves the electronic conductivity of the composite. The semicircle gradually decreases during the first ten cycles, indicating a decrease in R_{ct}. This means that the interface reaction kinetics becomes faster. Note that the inclined lines remain roughly parallel, that is the Li^+ diffusion is stable. The fitted R_{ct} of T-Nb_2O_5@CS is 390 Ω before cycling, and then decreases to 263.6 Ω at the 1st cycle, and further to 170.2 Ω at the 5th cycle and 72.8 Ω at the 10th cycle. The above results demonstrate that T-Nb_2O_5@CS has an excellent and stable transport ability for electrons and Li^+. Faradaic reaction kinetics is fast, which well explains the superior rate capability of T-Nb_2O_5@CS.

To comprehensively understand the electrochemical reaction properties of T-Nb_2O_5@CS, a series of CV measurements were performed at different scanning rates (Fig. 5a). As the scanning rate increases, the reduction peaks and oxidation peaks become more prominent due to polarization. The electrochemical reaction process can be deduced by using a power law relationship (Eq. 2) to analyze the peak current (I) and scan rate (v):

$$i = av^b \tag{2}$$

where I represents the peak current. v is the scan rate. a and b stand for two adjustable parameters, corresponding to the intercept and slope of the log(i) ~ log(v) plot, b can disclose the reaction property, b approaches 1, which means a pseudocapacitive behavior-dominated reaction process, and b is close to 0.5, which indicates a diffusive behavior-controlled reaction process. The log I versus log v plots are shown in Fig. 5b. The b values of the two anodic peaks and the one

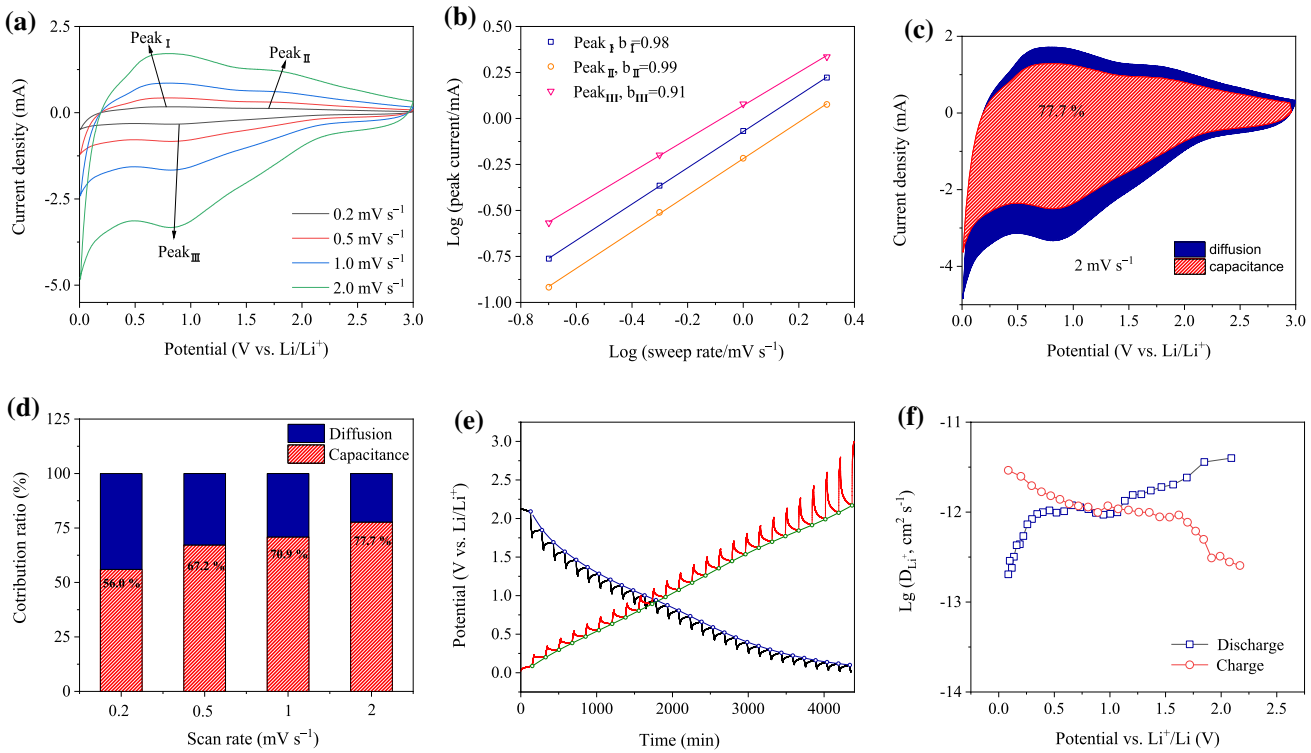

Fig. 5 (a) CV curves of T-Nb_2O_5@CS at scan rates from 0.2 mV s^{-1} to 2.0 mV s^{-1}, (b) relationship between log I versus log v for anodic and cathodic peaks, (c) separation of capacitive current and diffusive current at a scan rate of 2.0 mV s^{-1}, (d) column graphs of capacitive contribution ratios of T-Nb_2O_5@CS at different scan rates, (e) GITT curves of T-Nb_2O_5@CS; (f) Li^+ diffusion coefficients of T-Nb_2O_5@CS calculated by GITT as a function of potential.

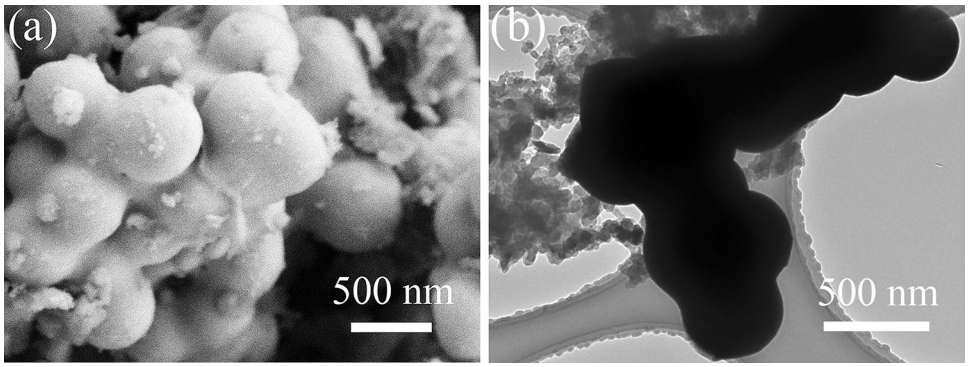

Fig. 6 (a) SEM and (b) TEM images of T-Nb_2O_5@CS after 600 cycles at 1 A g^{-1}.

cathodic peak are 0.98, 0.99, and 0.91, respectively. The high *b* value demonstrates that pseudocapacitive behavior dominates the electrochemical reaction of T-Nb_2O_5@CS. Furthermore, Eq. 3 can divide the current response of the CV curve into a pseudocapacitive current (k_1v) and diffusive current ($k_2v^{1/2}$) to quantify the influence of the two behaviors:

$$i = k_1 v + k_2 v^{1/2} \tag{3}$$

where k_1 and k_2 are two constants, calculated from the slope and intercept of the $I/v^{1/2}$ and $v^{1/2}$ plot. The CV curve at 2 mV^{-1} with the pseudocapacitive current and the diffusive current is displayed in Fig. 5c. Figure 5d indicates that the capacitive contribution accounts for 56.0%, 67.2%, 70.9%, and 77.7%, when the scanning rate is 0.2 mV s^{-1}, 0.5 mV s^{-1}, 1 mV s^{-1}, and 2 mV s^{-1}, respectively. The strong pseudocapacitive effect can result in a fast electrochemical reaction, which is consistent with the excellent rate capability of T-Nb_2O_5@CS. Usually, the high proportion of the pseudocapacitive effect is derived from the large surface area. The hybrid spheres are solid and their surface area is limited. Their strong pseudocapacitive effect should be attributed to the amorphous carbon within the hybrid spheres. It constructs an efficient network to transfer Li^+ and electrons, and achieve fast Li^+ insertion/extraction. The strong pseudocapacitive effect is also related to the small size of Nb_2O_5 nanocrystals, which reduces the diffusion distance of Li^+.

GITT was carried out to estimate Li^+ diffusion coefficients (D_{Li}) of T-Nb_2O_5@CS during the lithiation/discharge and de-lithiation/charge processes. GITT was tested by charging/discharging at 0.1 A g^{-1} for 20 min and then relaxation for 130 min. As shown in Fig. 5e, the overpotential is relatively low. D_{Li} was calculated based on Fick's second law of diffusion:

$$D_{Li} = 4/\pi\tau \times \left(m_B V_m / M_B S\right)^2 \times (\Delta E_s / \Delta E_\tau) \tag{4}$$

where *S* is the area of the electrode. m_B, M_B, V_m represent the actual mass, molar mass, and molar volume of the active material, respectively, τ stands for the pulse duration time, ΔE_τ represents the transient voltage change after eliminating the IR drop, and ΔE_s is the open-circuit voltage change. The potential-dependent D_{Li} is shown in Fig. 5f. D_{Li} ranges from $10^{-11.4}$ to $10^{-12.7}$ cm^2 s^{-1} in the lithiation/discharge stage. In the delithiation/charge stage, D_{Li} ranges from $10^{-11.5}$ to $10^{-12.6}$ cm^2 s^{-1}. This is higher than the 10^{-13} cm^2 s^{-1} of oxygen vacancy-mediated T-Nb_2O_5,[31] 10^{-14} cm^2 s^{-1} of the Nb_2O_5/carbon submicrostructures,[32] 10^{-13} cm^2 s^{-1} of C-Nb_2O_5.[27] The fast Li^+ diffusion is consistent with the EIS results and rate performance of T-Nb_2O_5@CS.

To gain insight into the cycling stability of T-Nb_2O_5@CS, we disassembled a coin cell after 600 cycles and then characterized the working electrode. The SEM image (Fig. 6a) and TEM image (Fig. 6b) indicate that, after the long-term charge–discharge cycles, the hybrid spheres are well retained and no structure collapse is observed, exhibiting good structural integrity. The robust hybrid spheres convincingly explain the excellent cycling stability of T-Nb_2O_5@CS.

There are several reasons for the improved electrochemical performance of T-Nb_2O_5@CS. First, the well-designed hydrolysis process and the strong adsorption effect of oleylamine greatly limit the hydrolysis rate of niobium ethoxide, resulting in very small hydrolysis products. Secondly, the hydrolyzed products are assembled into spheres by the oleylamine, which further brings about several structure advantages: (1) Oleylamine encapsulates the hydrolyzed products, which effectively limits the growth of T-Nb_2O_5 during hydrolysis and carbonization, and ensures the nanocrystal structure of T-Nb_2O_5, (2) the surface of the hybrid spheres is covered with a layer of amorphous carbon, which limits irreversible side reactions between Nb_2O_5 with the electrolyte, and (3) the surface carbon and internal carbon of the hybrid spheres construct efficient networks for Li^+ and electrons, which results in fast electron/Li^+ transfer and the outstanding structural stability of T-Nb_2O_5.

Conclusions

A simple strategy has been designed to construct T-Nb_2O_5@CS hybrid spheres, based on the controlled hydrolysis of niobium ethoxide as well as the intensive adsorption of oleylamine. This allows the T-Nb_2O_5 nanocrystals and amorphous carbon to be assembled to hybrid spheres. T-Nb_2O_5@CS exhibits excellent cycling performance as an anode material for LIBs, delivering a specific capacity of 279 mAh g^{-1} after 600 cycles at 1 A g^{-1} (5C). Rate performance is also outstanding, sustaining an average capacity of 186 mAh g^{-1} at 5 A g^{-1} (25C). Moreover, T-Nb_2O_5@CS also displays low electrochemical impedance, a high Li^+ diffusion coefficient, and remarkable capacitive effect in electrochemical reactions. The excellent electrochemical performance is mainly attributed to the T-Nb_2O_5 nanocrystals and carbon hybrid structure. The ultrafine size of the leads to high electrochemical activity. The surface carbon and internal carbon in the hybrid spheres prevent T-Nb_2O_5 from continuously consuming the electrolyte and constructing channel networks to transfer electrons and Li^+.

Conflict of interest On behalf of all authors, the corresponding author states that there is no conflict of interest.

References

1. C. Cai, Z.J. Yao, J.Y. Xiang, X.H. Chang, W.L. Yao, L.X. He, L.F. Ruan, Z.H. Chen, J.T. Shi, T.C. Liu, S.H. Shen, H.J. Xie, and Y.F. Yang, Rational construction of metal-organic framework derived dual-phase doping N-TiO_2 plus S-carbon yolk-shell nanodisks for high-performance lithium ion batteries. *Electrochim. Acta* 452, 142323 (2023).
2. B. Bai, L.L. Qiu, Y. Wang, X.Y. Jiang, J.X. Shui, Y.F. Yuan, L.X. Song, J. Xiong, and P.F. Du, Ultrafine carbon-nanofiber-reinforced graphene fiber electrodes for flexible supercapacitors with high specific capacitance and durable cycle stability. *ACS Appl. Energy Mater.* 6, 353 (2023).
3. Y.F. Zhang, Z.Y. Zeng, and H. Li, Design of 3d transition metal anchored B_5N_3 catalysts for electrochemical CO_2 reduction to methane. *J. Mater. Chem. A* 10, 9737 (2022).
4. S.H. Gong, B.Q. Wang, Y. Xue, Q.S. Sun, J. Wang, J. Kuai, F. Liu, and J.P. Cheng, $NiCoO_2$ and polypyrrole decorated three-dimensional carbon nanofiber network with coaxial cable-like structure for high-performance supercapacitors. *J. Colloid Interface Sci.* 628, 343 (2022).
5. L.X. He, L.F. Ruan, W.L. Yao, C. Cai, Z.H. Chen, X.H. Chang, J.T. Shi, T.C. Liu, S.H. Shen, Z.J. Yao, and Y.F. Yang, Tailoring sodium iron hexacyanoferrate/carbon nanotube arrays with 3D networks for efficient sodium ion storage. *J. Electron. Mater.* 52, 3517 (2023).
6. W.D. Wang, P.P. Zhang, S.Q. Gao, B.Q. Wang, X.C. Wang, M. Li, F. Liu, and J.P. Cheng, Core-shell nanowires of $NiCo_2O_4$@alpha-$Co(OH)_2$ on Ni foam with enhanced performances for supercapacitors. *J. Colloid Interf. Sci.* 579, 71 (2020).
7. C. Li, C. Zheng, F. Cao, Y.Q. Zhang, and X.H. Xia, The development trend of graphene derivatives. *J. Electron. Mater.* 51, 4107 (2022).
8. T. Zhang, Y.F. Yuan, B.X. Wang, G.S. Cai, P.F. Du, Y.Z. Huang, and S.Y. Guo, CoSe nanoparticles in-situ grown in 3D honeycomb carbon for high-performance lithium storage. *J. Colloid Interf. Sci.* 640, 52 (2023).
9. S.H. Shen, Y.B. Chen, J.C. Zhou, H.M. Zhang, X.H. Xia, Y.F. Yang, Y.Q. Zhang, A. Noori, M.F. Mousavi, M.H. Chen, Y. Xia, and W.K. Zhang, Microbe-mediated biosynthesis of multidimensional carbon-based materials for energy storage applications. Adv. Energy Mater. 2204259 (2023).
10. J. Fang, Y.F. Yuan, L.K. Wang, H.L. Ni, H.L. Zhu, J.L. Yang, J.S. Gui, Y.B. Chen, and S.Y. Guo, Synthesis and electrochemical performances of ZnO/MnO_2 sea urchin-like sleeve array as anode materials for lithium-ion batteries. *Electrochim. Acta* 112, 364 (2014).
11. T.F. Zhang, C. Li, F. Wang, A.H. Noori, M.F. Mousavi, X.H. Xia, and Y.Q. Zhang, Recent advances in carbon anodes for sodium-ion batteries. *Chem. Rec.* 22, e202200083 (2022).
12. F. Chen, Y.F. Yuan, L.W. Ye, M. Zhu, G.C. Cai, S.M. Yin, J.L. Yang, and S.Y. Guo, Co_3O_4 nanocrystalline-assembled mesoporous hollow polyhedron nanocage-in-nanocage as improved performance anode for lithium-ion batteries. *Mater. Lett.* 237, 213 (2019).
13. S.M. Zhang, G.L. Liu, W.M. Qiao, J.T. Wang, and L.C. Ling, Oxygen vacancies enhance the lithium ion intercalation pseudocapacitive properties of orthorhombic niobium pentoxide. *J. Colloid Interf. Sci.* 562, 193 (2020).
14. H.B. Ding, Z.H. Song, K. Feng, H.Z. Zhang, H.M. Zhang, and X.F. Li, Controlled synthesis of pure-phase metastable tetragonal Nb_2O_5 anode material for high-performance lithium batteries. *J. Solid State Chem.* 299, 122136 (2021).
15. W.X. Zhang, P.X. Shen, L.Z. Qian, P.C. Mao, M. Ahmad, H.T. Chu, R.G. Zheng, Z.Y. Wang, L. Bai, H.Y. Sun, Y.L. Yu, and Y.G. Liu, Tuning the phase composition in polymorphic Nb_2O_5 nanoplates for rapid and stable lithium ion storage. *Electrochim. Acta* 399, 139368 (2021).
16. J. Lin, S.Y. Zhao, T.G. Tranter, Z.Y. Zhang, F. Peng, D. Brett, R. Jervis, and P.R. Shearing, Modelling and experimental investigation of Nb_2O_5 as a high-rate battery anode material. *Electrochim. Acta* 443, 141983 (2023).
17. J.J. Yuan, X.F. Li, J. Liu, S.Y. Zuo, X.K. Li, F.K. Li, Y.F. Gan, H.S. He, X.J. Xu, X.K. Zhang, and J.X. Meng, Pomegranate-like structured Nb_2O_5/Carbon@N-doped carbon composites as ultrastable anode for advanced sodium/potassium-ion batteries. *J. Colloid Interf. Sci.* 613, 84 (2022).
18. X. Liu, G. Liu, H. Chen, J. Ma, and R. Zhang, Facile synthesis of Nb_2O_5 nanobelts assembled from nanorods and their applications in lithium ion batteries. *J. Phys. Chem. Solids* 111, 8 (2017).
19. Y.J. Yoo, and Y.C. Kang, Mesoporous Nb_2O_5 microspheres with filled and yolk-shell structure as anode materials for lithium-ion batteries. *J. Alloys Compd.* 776, 722 (2019).
20. X.X. Qu, B.L. Xing, G.X. Huang, H.H. Zhao, Z.D. Jiang, C.X. Zhang, S.W. Hong, and Y.J. Cao, Facile synthesis of flower-like T-Nb_2O_5 nanostructures as anode materials for lithium-ion battery. *J. Mater. Sci. Mater. Electron* 32, 875 (2021).
21. B.H. Deng, T.Y. Lei, W.H. Zhu, L. Xiao, and J.P. Liu, In-plane assembled orthorhombic Nb_2O_5 nanorod films with high-rate Li^+ intercalation for high-performance flexible Li-ion capacitors. *Adv. Funct. Mater.* 28, 1704330 (2018).
22. X.Y. Han, P.A. Russo, N. Goubard-Bretesche, S. Patane, S. Santangelo, R. Zhang, and N. Pinna, Exploiting the condensation reactions of acetophenone to engineer carbon-encapsulated Nb_2O_5 nanocrystals for high-performance Li and Na energy storage systems. *Adv. Energy Mater.* 9, 1902813 (2019).

23. Q. Wang, Z.Y. Jia, L.G. Li, J. Wang, G.G. Xu, X.Y. Ding, N. Liu, M.N. Liu, and Y.G. Zhang, Coupling niobia nanorods with a multicomponent carbon network for high power lithium-ion batteries. *ACS Appl. Mater. Interfaces* 11, 44196 (2019).
24. J.J. Hu, J.J. Li, K. Wang, and H.Y. Xia, Self-assembly Nb_2O_5 microsphere with hollow and carbon coated structure as high rate capability lithium-ion electrode materials. *Electrochim. Acta* 331, 135364 (2020).
25. Y.L. Yu, Y.H. Jin, N. Hasan, S.F. Cao, X.L. Wang, H. Ming, P.X. Shen, R.G. Zheng, H.Y. Sun, and M. Ahmad, Tuning the interface interaction between Nb_2O_5 nanosheets/graphene for high current rate and long cyclic lithium-ion batteries. *Electrochim. Acta* 435, 141397 (2022).
26. Z. Zhu, Y.G. Chen, F. Liu, H. Wang, R.H. Yu, D.Q. He, and J.S. Wu, Al-doped Nb_2O_5/carbon micro-particles anodes for high rate lithium-ion batteries. *Electrochim. Acta* 441, 141796 (2023).
27. X.L. Chen, K. Liu, Q.W. Qin, Z.L. Yu, M.Q. Li, X.Y. Qu, Y. Zhou, A.C. Dou, M.R. Su, and Y.J. Liu, High-rate capability of carbon-coated micron-sized hexagonal TT-Nb_2O_5 composites for lithium-ion battery. *Ceram. Int.* 47, 15400 (2021).
28. W. Fang, Y. Zhang, C. Kang, Q. Meng, A.R. Shi, S.F. Lou, X.Q. Cheng, G.P. Yin, and L.L. Zhang, Oxygen vacancies Nb_2O_{5-x}: ultrastable lithium storage anode materials for advanced rechargeable batteries. *Appl. Surf. Sci.* 600, 154068 (2022).
29. H.L. Cui, G.L. Zhu, Y.A. Xie, W. Zhao, C.Y. Yang, T.Q. Lin, H. Gu, and F.Q. Huang, Black nanostructured Nb_2O_5 with improved solar absorption and enhanced photoelectrochemical water splitting. *J. Mater. Chem. A* 3, 11830 (2015).
30. N. Li, X.W. Lan, L.B. Wang, Y.J. Jiang, S.T. Guo, Y.Q. Li, and X.L. Hu, Precisely tunable T-Nb_2O_5 nanotubes via atomic layer deposition for fast-charging lithium-ion batteries. *ACS Appl. Mater. Interfaces* 13, 16445 (2021).
31. Y.J. Zheng, Z.G. Yao, Z. Shadike, M. Lei, J.J. Liu, and C.L. Li, Defect-concentration-mediated T-Nb_2O_5 anodes for durable and fast-charging Li-ion batteries. *Adv. Funct. Mater.* 32, 2107060 (2022).
32. J.J. Yuan, H.S. He, X.F. Li, Y.F. Gan, M.Q. Mu, H.J. Yu, F. Kuang, X.K. Li, X.K. Zhang, and J. Liu, Fabrication of Nb_2O_5/Carbon submicrostructures for advanced lithium-ion battery anodes. *Chem. Eur. J.* 28, e202202432 (2022).
33. S.Y. Zhu, Y.J. Yang, J.Q. Liu, and J.M. Sun, Carbon-confined ultrasmall T-Nb_2O_5 nanocrystals anchored on carbon nanotubes by pyrolysing MLD-niobiumcone films for enhanced electrochemical applications. *J. Mater. Chem. A* 8, 25371 (2020).
34. Z.H. Song, H. Li, W. Liu, H.Z. Zhang, J.W. Yan, Y.F. Tang, J.Y. Huang, H.M. Zhang, and X.F. Li, Ultrafast and stable Li-(de) intercalation in a large single crystal H-Nb_2O_5 anode via optimizing the homogeneity of electron and ion transport. *Adv. Mater.* 32, 2001001 (2020).
35. S.Y. Zhu, P.H. Xu, J.Q. Liu, and J.M. Sun, Atomic layer deposition and structure optimization of ultrathin Nb_2O_5 films on carbon nanotubes for high-rate and long-life lithium ion storage. *Electrochim. Acta* 331, 135268 (2020).
36. S.H. Shen, S.Z. Zhang, X. Cao, S.J. Deng, G.X. Pan, Q. Liu, X.L. Wang, X.H. Xia, and J.P. Tu, Popcorn-like niobium oxide with cloned hierarchical architecture as advanced anode for solid-state lithium ion batteries. *Energy Storage Mater.* 25, 695 (2020).
37. X.M. Zhai, J.L. Liu, Y.J. Zhao, C. Chen, X.C. Zhao, J.B. Li, and H.B. Jin, Oxygen vacancy boosted the electrochemistry performance of Ti^{4+} doped Nb_2O_5 toward lithium ion battery. *Appl. Surf. Sci.* 499, 143905 (2020).
38. X.X. Qu, Y.H. Liu, B.B. Li, B.L. Xing, G.X. Huang, C.X. Zhang, S.W. Hong, J.L. Yu, and Y.J. Cao, Synthesis of high reversibility anode composite materials using T-Nb_2O_5 and coal-based graphite for lithium-ion battery applications. *Energy Fuels* 34, 3887 (2020).
39. Z.Q. Hu, Q. He, Z. Liu, X. Liu, M.S. Qin, B. Wen, W.C. Shi, Y. Zhao, Q. Li, and L.Q. Mai, Facile formation of tetragonal-Nb_2O_5 microspheres for high-rate and stable lithium storage with high areal capacity. *Sci. Bull.* 65, 1154 (2020).
40. J.W. Kang, H.W. Zhang, Z.Y. Zhan, Y.Q. Li, M. Ling, and X.H. Gao, Construction of a flexible Nb_2O_5/carboxyl multiwalled carbon nanotube film as anode for lithium and sodium storages. *ACS Appl. Energy Mater.* 3, 11841 (2020).
41. R. Kang, S. Li, B.B. Zou, X.H. Liu, Y. Zhao, J.X. Qiu, G.C. Li, F. Qiao, and J.B. Lian, Design of Nb_2O_5@rGO composites to optimize the lithium-ion storage performance. *J. Alloys Compd.* 865, 158824 (2021).
42. J.B. Wu, Y. Lin, and X.H. Huang, Aspergillus oryzae spore carbon/niobium oxide composite material as anode for lithium ion batteries. *Mater. Res. Bull.* 134, 111062 (2021).
43. H.F. Yu, L. Xu, H.Y. Wang, H. Jiang, and C.Z. Li, Nanochannel-confined synthesis of Nb_2O_5/CNTs nanopeapods for ultrastable lithium storage. *Electrochim. Acta* 295, 829 (2019).
44. K. Kim, J. Hwang, H. Seo, H.S. Kim, and J.H. Kim, Surface-controlled Nb_2O_5 nanoparticle networks for fast Li transport and storage. *J. Mater. Sci.* 54, 2493 (2019).